Matuhina, Anastasia; Grandhi, G. Krishnamurthy; Pan, Fang; Liu, Maning; Ali-Löytty, Harri; Ayedh, Hussein M.; Tukiainen, Antti; Smått, Jan-Henrik; Vähänissi, Ville; Savin, Hele; Li, Jingrui; Rinke, Patrick; Vivo, Paola

Role of CsMnCl3 Nanocrystal Structure on Its Luminescence Properties

Published in:
ACS Applied Nano Materials

DOI:
10.1021/acsanm.2c04342

Published: 27/01/2023

Document Version
Publisher's PDF, also known as Version of record

ACS APPLIED NANO MATERIALS

www.acsanm.org Article

Role of $CsMnCl_3$ Nanocrystal Structure on Its Luminescence Properties

Anastasia Matuhina, G. Krishnamurthy Grandhi,* Fang Pan, Maning Liu, Harri Ali-Löytty, Hussein M. Ayedh, Antti Tukiainen, Jan-Henrik Smått, Ville Vähänissi, Hele Savin, Jingrui Li, Patrick Rinke, and Paola Vivo*

Cite This: *ACS Appl. Nano Mater.* 2023, 6, 953−965 Read Online

ACCESS | Metrics & More | Article Recommendations | Supporting Information

ABSTRACT: Cesium manganese chloride ($CsMnCl_3$) nanocrystals (NCs) have recently been recognized as potential lead-free perovskite candidates for red emission. To ascertain how the luminescence properties depend on the NC structures formed under different synthesis conditions, we synthesized $CsMnCl_3$ NCs in two polymorphic structures, namely, cubic (c-$CsMnCl_3$) and rhombohedral (r-$CsMnCl_3$), by tuning the reaction temperature of a hot injection route. c-$CsMnCl_3$ NCs are found to be nonemissive, whereas r-$CsMnCl_3$ NCs exhibit red emission at 670 nm with a photoluminescence quantum yield of 40%. Density functional theory calculations reveal an indirect band gap for c-$CsMnCl_3$—the electronic transitions between valence and conduction band edges are prohibited by orbital symmetry and spin. Conversely, r-$CsMnCl_3$ NCs possess a direct band gap. Further, transient absorption measurements suggest self-trapped exciton formation in r-$CsMnCl_3$ NCs, which contributes to their emission characteristics. Our proof-of-concept demonstration of photocurrent generated from the emitting r-$CsMnCl_3$ NCs indicates their suitability for luminescent solar concentrator applications. The findings of this work highlight the importance of understanding structure-luminescence relationship of emerging lead-free perovskites providing design criteria for red-emitting materials.

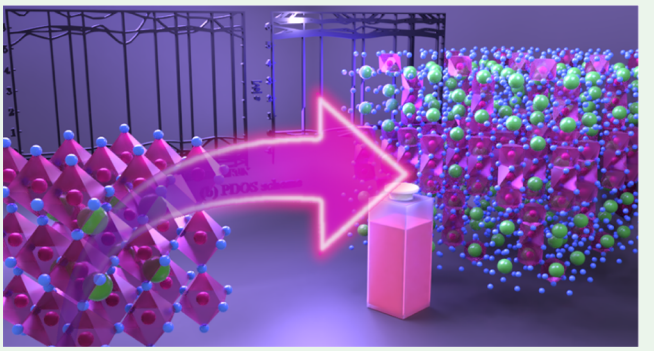

KEYWORDS: *lead-free perovskite, nanocrystals, $CsMnCl_3$, density functional theory, self-trapped exciton, structure−property relationship, luminescent solar concentrators*

INTRODUCTION

Three-dimensional (3D) lead-halide perovskite (LHP) nanocrystals (NCs) are promising for photonic and light-emitting applications due to their broad-range absorption, tunable emission energies within a wide range of colors, and high color purity [narrow emission full width at half-maximum (fwhm)].[1] Near-unity photoluminescence (PL) quantum yield (QY) has been achieved in blue, green, and red spectral regions for all-inorganic $CsPbX_3$ (X = Cl, Br, or I) NCs.[2] However, red-emissive $CsPbI_3$ NCs (emission maximum ∼620−690 nm)[3] have proven to be inherently phase unstable. Moreover, the toxicity of water-soluble Pb^{2+} in LHP NCs has recently triggered the search and subsequent discovery of Pb-free metal-halide NCs, typically based on Bi, Sb, and Cu, with a maximum PLQY of 97% for $Cs_3Cu_2I_5$ in the deep-blue spectral region.[4,5] Nevertheless, none of the reported Pb-free NCs have so far simultaneously exhibited high PLQY and stable red emission beyond 650 nm.

Cesium manganese halides ($CsMnBr_3$ and $CsMnCl_3$) with one-dimensional (1D) Mn−Cl chains in their structure are an interesting family of emerging Pb-free NCs displaying high absorption coefficients, Stokes-shifted and tunable emission, and PLQYs up to ∼50%.[6−8] In particular, $CsMnCl_3$ NCs are intriguing as contradictory emission properties have been outlined so far. While the initial works by Gao et al.[9] and Feng et al.[10] reported nonemissive properties, Guan et al. and Hao et al. demonstrated $CsMnCl_3$ NCs with red emission centered at 654−660 nm.[8,11] Guan and co-workers synthesized $CsMnCl_3$ NCs with emission at 660 nm and a PLQY of 0.7% through a modified hot injection approach.[11] The authors indicated a deviation from the 1:1:3 stoichiometry, which might explain the low PLQY. Hao and colleagues synthesized $CsMnCl_3$ NCs through the benzoyl chloride injection route and doped them with Zn^{2+} ions to improve their PLQY from

Received: October 3, 2022
Accepted: December 28, 2022
Published: January 5, 2023

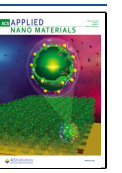

56 to 77%.[8] The inconsistency in the emission properties of $CsMnCl_3$ NCs (being emissive and nonemissive) needs to be yet clarified.

Variations in the crystal phase or the local lattice symmetry[9,10] may explain the contradicting luminescence behavior reported for $CsMnCl_3$ NCs. Examples in the literature for both Pb-based and Pb-free perovskites support this argument.[12−14] The electronic structures of LHPs can be altered by both intrinsic (e.g., defects) and extrinsic (such as temperature, pressure, and light) factors that promote transition between different crystal phases (such as cubic, tetragonal, orthorhombic, and hexagonal).[12,13] For instance, complete PL quenching of $CsPbBr_3$ NCs is observed upon applying high pressure, which tilts the lead bromide octahedra and changes the band gap form direct to indirect.[13] For Pb-free $Cs_2AgInCl_6$, Luo et al. demonstrated that breaking its crystal inversion symmetry facilitates radiative recombination, resulting in bright white light emission.[14] These examples highlight the importance of thoroughly identifying the structure-luminescence relationships[15,16] to discover unexpected properties of halide perovskites and promote new optoelectronic applications. However, being an emerging family of materials, only few structure-luminescence studies exist for Pb-free perovskites, thus explaining the still limited understanding of their electronic band structures.[17]

To elucidate the dependence of the luminescence properties of $CsMnCl_3$ NCs on the structural parameters, we report the synthesis of these Pb-free NCs in two different crystal phases produced via the hot injection route, which is a well-known approach for the phase control of NCs.[18−21] The formation of cubic (c-) and rhombohedral (r-) phases of $CsMnCl_3$ NCs is demonstrated by the structural refinement of their X-ray diffraction (XRD) patterns. The two phases exhibit striking differences in luminescence properties, which are rationalized through the study of their electronic band structures by density functional theory (DFT) calculations. The high exciton binding energy of r-$CsMnCl_3$ NCs ensures a relatively bright emission (PLQY = 40%) with a maximum at 670 nm, which is highly Stokes-shifted from their band gap. In addition, transient absorption (TA) measurements reveal the ultrafast relaxation dynamics of the NCs in their excited state, which influences their emission properties. Furthermore, we study the applicability of the r-$CsMnCl_3$ NCs possessing the Stokes-shifted emission and the excellent phase stability for energy harvesting in proof-of-concept luminescent solar concentrators (LSCs). Overall, by establishing a structure-luminescence relationship for the emerging class of manganese chloride compounds, this work may contribute to the understanding of the emission properties of other metal-based Pb-free halide perovskites and inspire the design of new highly luminescent materials.

EXPERIMENTAL SECTION

Materials. Cesium carbonate (Cs_2CO_3, 99.9%), octadecene (ODE, 90%), oleic acid (OA, 90%), oleylamine (OlAm, technical grade, 70%), Mn (II) chloride ($MnCl_2$, 99%), hexane (≥95%), and methyl acetate (MeOAc, ≥98%) were purchased from Sigma-Aldrich. A conventional distillation process was carried out to obtain anhydrous MeOAC. All other chemicals were used without further purification.

Preparation of Cs-Oleate. Cs_2CO_3 (407 mg) was loaded into a 50 mL three-neck flask along with ODE (18 mL). The solution was degassed for 1 h at 120 °C. Dry OA (1.74 mL) was then injected under argon (Ar) upon an additional 15 min of degassing. At this point, the temperature was increased to 150 °C to dissolve Cs_2CO_3 and form a fully transparent Cs-oleate solution.

The Cs-oleate precursor was cooled down to room temperature and stored under vacuum for further use. Before the injection, Cs-oleate solution was degassed for at least 30 min at 120 °C and heated up to 150 °C under Ar.

Synthesis of $CsMnCl_3$ NCs. $CsMnCl_3$ NCs were synthesized following a modified protocol.[22] Anhydrous $MnCl_2$ (156 mg) was loaded into a 25 mL three-neck flask along with dry ODE (10 mL), dry OA (2 mL), and dry OlAm (2 mL). The scaling and handling were carried out in an inert atmosphere. The halide precursor solution was degassed under vacuum for 1.5 h at 120 °C. During the heating and degassing processes, the solution gradually turns color from reddish-brown to transparent yellow (Figure S1a). The temperature of the reaction flask was increased to the desired values (e.g., 150, 180, and 200 °C) under Ar gas, and Cs-oleate solution (i.e., 2, 3, and 4 mL which corresponds to 0.7, 0.5 and 0.35 Mn to Cs ratio) was swiftly injected into the flask under vigorous stirring. There was no obvious color change observed after the injection. The reaction was kept at the injection temperature for 5 s and then quickly quenched by an ice-water bath (Figure S1b). The crude solution was purified by centrifugation at 8550 rpm for 5 min without any antisolvent. The as-obtained white-pinkish precipitate (Figure S1c) emitted strong pink-red light under the UV lamp. After discarding the supernatant, the vials with the remaining NC precipitate were dried in a vacuum desiccator (typically overnight) to remove the excess solvent. The dry NC precipitate was redispersed in hexane for further use. All NC suspensions displayed high colloidal stability. Importantly, the nonpurified $CsMnCl_3$ NCs were degrading quickly and changing color to black (Figure S1d).

Purification of $CsMnCl_3$ NCs. To efficiently isolate the NCs from the solution and remove the excess of the ligands on their surface, different purification methods were tested. For example, after the first purification step described above, the NCs dispersed in 2 mL of hexane were centrifuged with varying speeds ranging from 8600 to 14,000 rpm. However, no visible precipitation of the NCs was observed.

A series of antisolvents were also tested. The crude solution was divided into equal parts and one portion of anhydrous isopropanol or anhydrous ethyl acetate was added to two portions of the NC dispersion. However, the resultant precipitate did not show any visible PL emission. Nevertheless, adding anhydrous MeOAC in 1:1 volume ratio to prepurified NC suspension, followed by centrifugation at 12,000 rpm, resulted in the formation of a white-pinkish NC precipitate with structural and optical properties similar to the one obtained after the first purification step.

Characterization Techniques. XRD patterns were recorded by a Malvern Panalytical Empyrean Alpha 1 diffractometer in the powder diffraction mode using Cu Kα radiation (λ = 1.5406 Å) and a cathode voltage and current of 45 kV and 40 mA, respectively. High-resolution XRD patterns were obtained for all samples under identical measurement settings (4−62° range, 0.0262° step size, and 17 s per step). Samples were prepared by drop-casting from the as-synthesized dispersions on precleaned microscopy cover glasses (20 × 20 mm). To ensure a proper comparison between the samples while guaranteeing a reasonable signal-to-noise ratio, a similar thickness was used for all samples. The structural information was derived from Rietveld refinement using Malvern Panalytical's HighScore software. A three-dimensional visualization system for electronic and structural analysis (VESTA) was used to draw the crystal structures.[23]

Transmission electron microscope (TEM) images were taken using a JEM-F200 microscope (200 kV). 20 μL of the NC dispersion in hexane (the absorbance at 280 nm was set to 0.2) was drop-casted on the carbon-coated Cu grids. Ultraviolet−visible (UV−vis) absorption spectra were recorded using a Shimadzu UV-3600 UV−vis−NIR spectrophotometer. Steady-state PL, absolute PLQYs, and time-resolved PL (TRPL) decays were measured using an FLS1000 spectrofluorometer (Edinburgh Instruments, UK) comprising a mountable integrating sphere and a microflash lamp (frequency 100 Hz). The stability of the optical properties was monitored using the

https://doi.org/10.1021/acsanm.2c04342
ACS Appl. Nano Mater. 2023, 6, 953−965

same diluted NC dispersions stored under ambient conditions (RH ∼ 40% T = 25 °C) in the dark.

Ultrafast TA measurements were conducted with a home-built TA spectrometer. The NC dispersion samples in a 2 mm thick quartz cuvette were excited by laser pulses at 300 nm (Libra F, Coherent Inc., coupled with Topas C, Light Conversion Ltd.), while a white continuum generator (heavy water) was employed to generate the probe beam. The TA responses (time resolution: ∼150 fs) were recorded using an ExciPro TA spectrometer (CDP, Inc.) equipped with a CCD array.

Inductively coupled plasma mass spectroscopy (ICP−MS) measurements were conducted with Thermo Scientific iCAP RQ equipment. After purification, NC precipitate samples were dissolved in concentrated HNO_3 followed by dilution and measurement in 2% HNO_3 matrix. Ionic standard solutions with a concentration range of 0.001−1000 μg/L for Cs and Mn were prepared in 2% HNO_3 using super-pure chemicals (Romil-SpA) and applied to measure calibration curves. Ultrapure H_2O (18.2 MΩ cm, Merck Milli-Q) was used for sample dilutions.

For low-temperature PL (LTPL) measurements of $CsMnCl_3$ NCs deposited on a silica substrate, the measurements were conducted in a cryostat (CTI CCS-150) at 20 K intervals from 30 to 293 K. The samples were excited by a 380 nm light-emitting diode (pE-4000—CoolLED) at 380 nm.

DFT Calculations. DFT calculations were carried out based on the measured crystal and atomic structure of both c- and r-$CsMnCl_3$ models. We first identified the most stable magnetic state of both structures. Then, we calculated the band structure based on the primitive cell models of these states. Specifically, the most stable magnetic state of c-$CsMnCl_3$ is the G-type antiferromagnetic one, in which the spin-up and -down Mn^{2+} ions adopt a face-centered cubic alignment with space group $Pm\bar{3}m$. The most stable magnetic state of r-$CsMnCl_3$ has the $R\bar{3}m$ symmetry.

To accurately calculate the electronic structure, we used the hybrid Heyd-Scuseria-Ernzerhof (HSE06) exchange−correlation functional in combination with the zero-order regular approximation to account for the scalar relativistic effects. For c-$CsMnCl_3$ ($Pm\bar{3}m$) and r-$CsMnCl_3$ ($R\bar{3}m$), we used Γ-centered 6 × 6 × 6 and 3 × 3 × 3 k-point meshes for the Brillouin-zone sampling, respectively.

LSC Setup. To explore the potential of $CsMnCl_3$ NCs in LSC devices, a dedicated experimental setup was built. The schematic illustration of our experimental setup including the proof-of-concept device is presented in the relevant chapter. The proof-of-concept device consists of a thin film of NCs deposited on top of a glass plate. The edge of this miniature window (∼2 cm × 0.15 cm) is placed directly on top of a silicon pn-junction photodiode (2 × 2 cm^2). An opaque cover is placed on top of the surrounding photodiode area. To eliminate the possible effect of background light, the photodiode is placed in a dark box. While in the box, a light beam with a spectrum similar to a warm white light-emitting diode (400−700 nm) collimated by a lens producing a spotlight with a diameter of ∼1.6 cm and a power of ∼9.5 mW is directed perpendicularly to the middle of the glass. The NCs on the glass surface absorb and re-emit some of the light that will reach the photodiode, where it will be absorbed and transformed into a photocurrent. The resulting I−V characteristics of the photodiode for an applied bias between −5 and 0.5 V were measured. Since the measured photodiode current is directly proportional to the intensity of the incident light, the configuration provides information on the intensity of the arriving light (i.e., light emitted by the NCs).

RESULTS AND DISCUSSION

$CsMnCl_3$ NCs were synthesized through conventional hot injection of Cs-oleate into a $MnCl_2$ precursor solution (see Experimental Section, Figures 1 and S1 for complete details).[10] To characterize the as-synthesized NCs, we purified and dispersed them in hexane. The injection temperature and the Mn/Cs precursor molar ratio were tailored in the range of 150−200 °C and 0.35−0.7, respectively. The selected injection

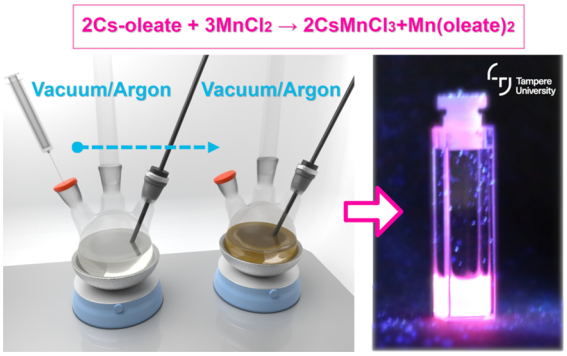

Figure 1. Schematic illustration of the NC synthesis via conventional hot injection method through the Cs-oleate route.

temperature range (150−200 °C) for the $CsMnCl_3$ NCs falls within the typical injection temperature range of the perovskite NCs of 120−250 °C. The injection temperature below the lower boundary of 150 °C resulted in no formation of the NCs in our synthesis. On the other hand, the NCs formed at 200 °C show significantly lower PLQY compared to the ones synthesized at 180 °C. The NCs synthesized at 150, 180, and 200 °C are hereafter referred to as 150@NCs, 180@NCs, and 200@NCs, respectively. Also, at the fixed injection temperature of 180 °C, the samples with varying Mn/Cs molar ratios (loading ratio) are labeled as 180@NCs//0.7, 180@NCs//0.5, and 180@NCs//0.35. The Mn/Cs ratio for 150@NCs and 200@NCs was fixed at 0.7.

Structural and Morphological Analysis of $CsMnCl_3$ NCs. The XRD patterns of all $CsMnCl_3$ NCs were recorded in ambient conditions (RH ∼ 40%, T = 25 °C) to study the effect of injection temperature and Mn/Cs ratio on their crystal structure, as shown in Figure 2. To interpret the distinct XRD pattern of 150@NCs, which is different from that of the other samples, we performed Rietveld refinement on all XRD patterns (Figure 2b−e,i). The very low values of goodness-of-fit (χ^2) and residual weighting factor (R_{wp}) confirm the reliability of the refined structural parameters (see Tables S1 and S2 for the refinement parameters). The 150@NC sample adopts a 3D cubic $CsMnCl_3$ perovskite phase with $Pm\bar{3}m$ space group. In the perovskite structure of $CsMnCl_3$, Cs^+ ions fill the voids created by the corner-shared $MnCl_6$ octahedra in all three crystal dimensions, as shown in Figure 2f. This crystal structure is identical to the perovskite structure of cubic $CsPbCl_3$. The perovskite phase of bulk $CsMnCl_3$ has earlier only been successfully synthesized at high pressures, in agreement with the $CsMnCl_3$ phase-temperature diagram.[24] We, however, obtained the cubic phase of $CsMnCl_3$ (c-$CsMnCl_3$) at the nanoscale at ambient pressures and at a low temperature of 150 °C. We hypothesize that the high surface energy associated with the small c-$CsMnCl_3$ NCs compared to their bulk counterparts (feature size of NCs is only 3.9 nm) balances the overall energy necessary to favor the formation of the perovskite structure at ambient pressure. In other words, c-$CsMnCl_3$ crystallizes in a kinetically trapped high-pressure structure.[25] While metal halides based on ions other than Pb^{2+}, Sn^{2+}, and Ge^{2+} usually do not crystallize in the 3D perovskite structure,[26] $CsMnCl_3$ can form a 3D structure even at ambient pressure. This emphasizes the versatility of manganese colloidal chemistry due to the unique size of Mn^{2+} (0.67−0.83 Å depending on the high- or low-spin coordination) with respect to Cl^- (1.81 Å) ions that enables the formation of both

https://doi.org/10.1021/acsanm.2c04342
ACS Appl. Nano Mater. 2023, 6, 953−965

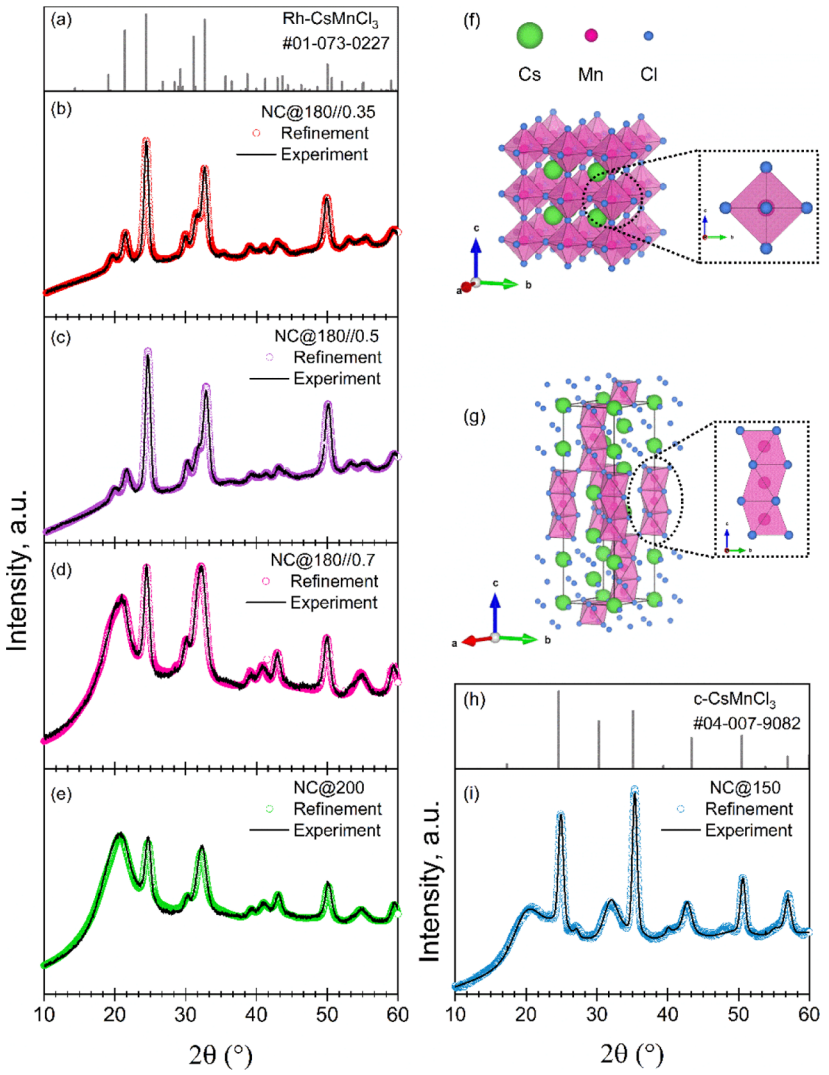

Figure 2. (a,h) Reference XRD patterns of c-$CsMnCl_3$ and r-$CsMnCl_3$ with reference codes 04-007-9082 and 01-073-02227, respectively. (b−e,i) Experimental (solid lines) and refined (open circles) profiles obtained after the full-pattern Rietveld refinement of the XRD patterns of 180@NCs//0.35, 180@NCs//0.5, 180@NCs//0.7, 200@NCs, and 150@NCs samples. The refined crystal structures of (f) c-$CsMnCl_3$ NCs and (g) r-$CsMnCl_3$ NCs. The corresponding insets display the repeating manganese iodide polyhedral unit of the structures.

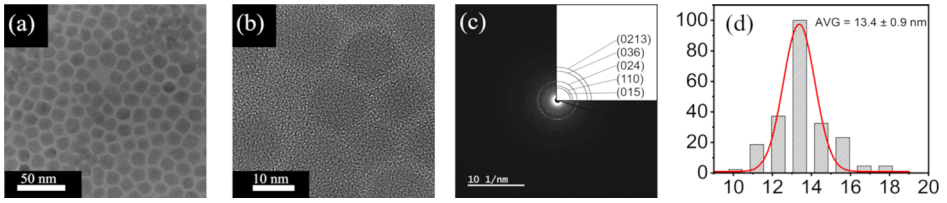

Figure 3. (a,b) TEM images of NCs@180//0.5 sample. (c) SAED pattern with assigned reflections. (d) Size distribution, determined as the diameter of the pentagons of NCs@180//0.5 sample.

perovskite and nonperovskite structures.[24] $CsMnCl_3$ NCs crystallize in a pure rhombohedral (nonperovskite) phase when the injection temperature is equal to or higher than 180 °C (Figure 2b−e). The space group of $R\bar{3}m$ of these NCs is the same as for the reported bulk $CsMnCl_3$.[27] In the crystal structure of r-$CsMnCl_3$ (Figure 2g), three face-sharing $MnCl_6$ octahedra form a 1D chain; these Mn_3Cl_{12} chains are further interconnected into a 3D framework via corner-sharing; the negatively charged framework binds the Cs^+ ions along the c-axis. The formation of r-$CsMnCl_3$ NCs instead of c-$CsMnCl_3$ NCs at higher injection temperatures is similar to the formation of the hexagonal structure of bulk $CsMnCl_3$ after heating its cubic structure at 300 °C for a few hours.[24] Similar injection temperature-dependent phase control has already been achieved in the case of Pb-based perovskite NCs.[19−21] The anticipated 1:1 Cs/Mn ratio of all NCs was further confirmed by ICP−MS (see Table S3).

The morphological evolution and size distribution of the synthesized NCs were studied by TEM, as shown in Figures 3, S2, and S3. The 150@NC sample exhibits a mixed morphology, with most of the particles having a rodlike shape. The morphology of the particles is dependent on the

https://doi.org/10.1021/acsanm.2c04342
ACS Appl. Nano Mater. 2023, 6, 953−965

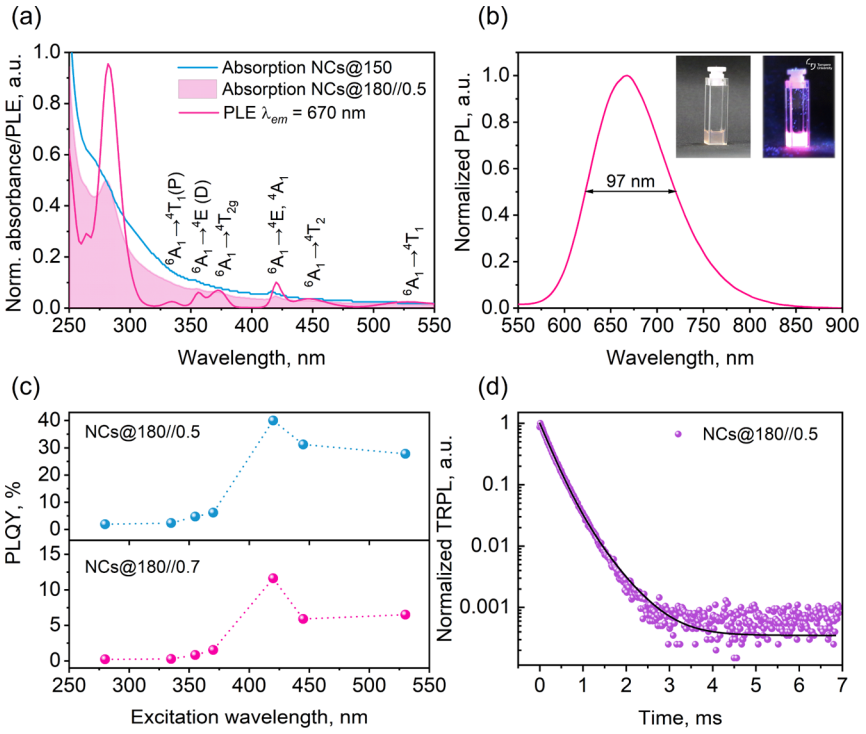

Figure 4. (a) Normalized absorption spectra of 150@NCs (c-$CsMnCl_3$) and 180@NCs//0.5 (r-$CsMnCl_3$) NCs along with the PLE spectrum of r-$CsMnCl_3$ NCs. (b) Normalized PL spectrum of r-$CsMnCl_3$ NCs. Inset: photos of the NCs in hexane under room (left) and UV (λ = 365 nm) lights (right). (c) Excitation wavelength-dependent PLQY of r-$CsMnCl_3$ NCs for two different Cs/Mn ratios. (d) TRPL decay of r-$CsMnCl_3$ NCs.

precursor ratio in the case of the 180@NC samples. Truncated sphere-shaped particles are obtained when the Mn/Cs ratio is 0.7 (Figure S2c). When decreasing the Mn/Cs ratio, the edges of the particles gradually become more defined and finally convert into hexagons when the ratio is 0.35. The average diameter of the hexagon- or sphere-like shaped particles varies from 10.8 ± 0.8 nm to 13.4 ± 1.0 nm, and the nanorods (150@NCs sample) are 3.9 ± 0.9 nm in length (see Figures 3 and S3).

Optical Properties and Electronic Band Structure from DFT. The key optical properties of the as-synthesized $CsMnCl_3$ NCs are presented in Figure 4a–d. The c-$CsMnCl_3$ and r-$CsMnCl_3$ NCs strongly absorb at 275 and 280 nm (Figure 4a), respectively. The c-$CsMnCl_3$ NCs (150@NCs) are nonemissive. On the contrary, the r-$CsMnCl_3$ NCs exhibit red emission centered at 670 nm (Figure 4b) with a PLQY of 40%. The corresponding Stokes shift between absorption and PL is 2.6 eV. The emission wavelength of 670 nm is the longest ever reported for these NCs. Guan and co-workers show the PL for the $CsMnCl_3$ NCs centered at 660 nm with a very low PLQY of 0.7%,[11] which can be partially attributed to the surface traps. Hao et al. synthesized the NCs through benzoyl chloride injection and achieved an improved PLQY of 56.3%,[8] which is the consequence of the excess chloride ions provided by the benzoyl chloride.[28,29] Nevertheless, the Cs-oleate injection route employed in this work might be preferable over the one involving hazardous benzoyl chloride when aiming at eco-friendly alternatives to LHP NCs. Further, the fwhm value of the NCs is 97 nm (Figure 4b), that is, comparable to the value reported in a previous study on these NCs.[11]

Absorption and PL excitation (PLE) spectra in the above-mentioned works are also depicted in a shorter wavelength range compared to our work. The corresponding optical band gap values for c-$CsMnCl_3$ and r-$CsMnCl_3$ NCs are 4.8 and 5.0 eV, respectively (see Figure S4b and Table S4 for Tauc plot analysis). The very large band gaps of the NCs are supported by their electronic band structures obtained from DFT calculations (see Figure 5).

The $MnCl_6$ octahedra in the case of the rhombohedral structure are slightly distorted, whereas the cubic one consists of undistorted octahedra. The octahedral distortion can be quantified using $D = \frac{1}{6}\sum_{i=1}^{i=6}\left(\frac{|l_i - l_{avg}|}{l_{avg}}\right)$,[30] where l_i is the bond lengths between Mn^{2+} and six Cl^- and l_{avg} is the average bond length. The octahedra in the rhombohedral structure are 7.8% distorted compared to the cubic structure. The local symmetry breaking, driven by dimensional reduction, may lead to the difference in the electronic structure of the two crystal phases of $CsMnCl_3$.[31]

To gain insight into the electronic structure of $CsMnCl_3$, we carried out first-principles DFT calculations based on the experimental structures of both 180@NCs//0.5 (rhombohedral structure, space group: $R\bar{3}m$) and 150@NCs (cubic structure, space group: $Pm\bar{3}m$). We used the hybrid HSE06 exchange–correlation functional[32] implemented in the all-electron numeric-atom-centered orbital code FHI-aims.[33−36] The default amount of 25% screened Hartree-Fock exchange in HSE06 facilitates a more accurate description of the materials' electronic structure including the on-site Coulomb interaction between the Mn 3d electrons.

Test calculations indicate that the G-type antiferromagnetic (AFM) state of c-$CsMnCl_3$ is the most stable, and similarly, r-$CsMnCl_3$ adopts an AFM configuration, in which the unpaired $3d^5$ electrons of nearest-neighbor Mn^{2+} cations have opposite spins. Figure 5a,b shows the band structures and projected densities-of-states (PDOS) of these two AFM structures.

https://doi.org/10.1021/acsanm.2c04342
ACS Appl. Nano Mater. 2023, 6, 953−965

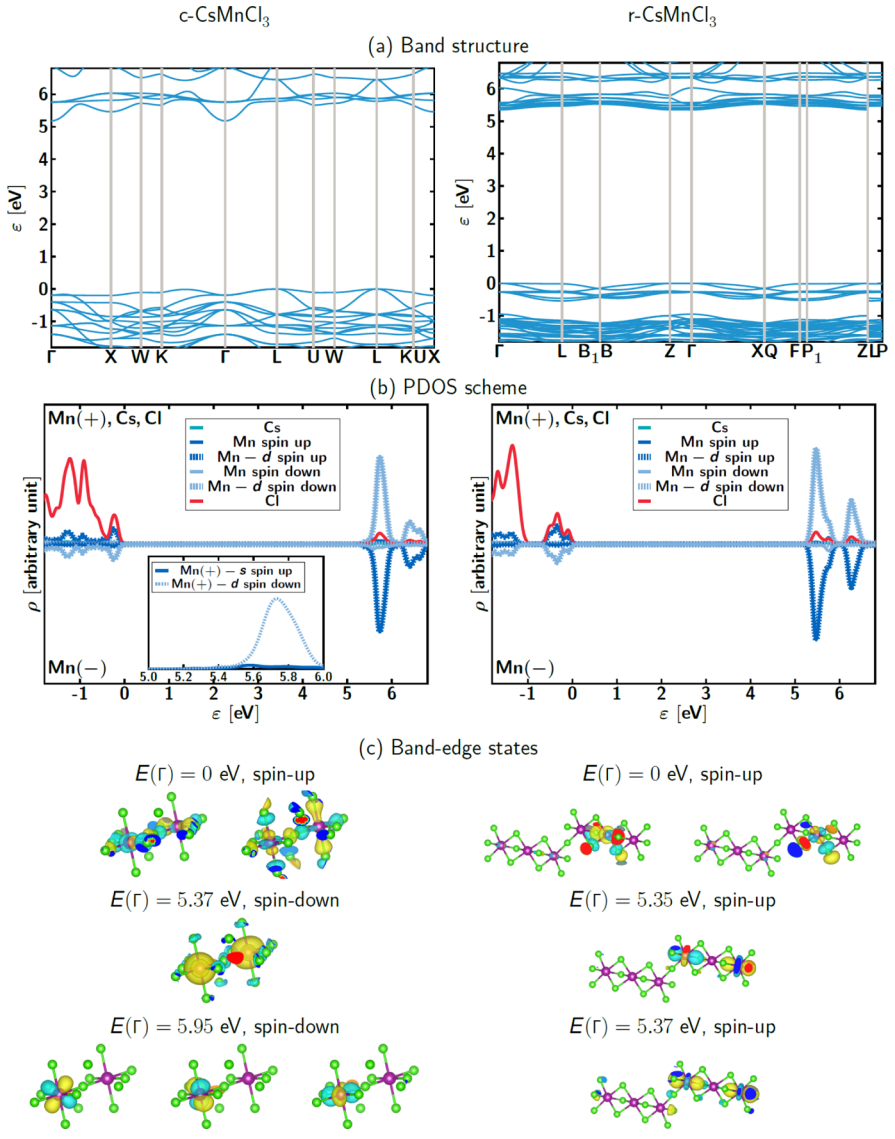

Figure 5. DFT-calculated electronic structure of AFM c-$CsMnCl_3$ (left column) and r-$CsMnCl_3$ (right column): (a) band structures, (b) PDOS schemes, and (c) wave functions of selected band-edge states at Γ. The VB maximum is shifted to 0 eV. In (a), only spin-up bands are shown as spin-down components exhibit the same structure. In (b), the spin-up DOS (identical to the spin-down counterparts) projected on both Cs and Cl species are colored in turquoise and red, respectively. Both spin-up (+) and spin-down (−) components (in blue and light blue, respectively) from a set of Mn^{2+} cations denoted by Mn(+) are shown in the upper panel, while the lower panel shows the Mn PDOS contributed by Mn(−) cations, the nearest neighbors of Mn(+). The d components of Mn PDOS are highlighted in dashed lines. In (c), the positive and negative parts of the wave functions are colored in cyan and yellow, respectively. Mn^{2+} and Cl^- ions are given in purple and light green, respectively, while the Cs^+ ions are not depicted for clarity.

These two polymorphs exhibit similar band gaps and similar valence band characters that consist of Cl-3p and Mn-3d orbitals. Figure 5c shows the wave functions for selected states. The plots of the valence band (VB) top at $E(\Gamma)$ = 0 eV show two degenerate bands: one with mainly Mn-$3d_{x^2-y^2}$ character and the other with Mn-$3d_{z^2}$.

Unlike in their VBs, c-$CsMnCl_3$ and r-$CsMnCl_3$ differ in their CBs (conduction bands). The CB minimum of c-$CsMnCl_3$ has a pronounced 4s character, which is highly dispersed (see Figure 5a left) and extends over a large energy range (see the inset of Figure 5b left). This results in an indirect band gap of 5.18 eV, which is noticeably smaller than the direct band gap (5.37 eV). More importantly, the electronic transitions between the d-type VB-top states and the s-type CB-bottom states are unfavorable. This agrees with the nonemissive behavior of the c-$CsMnCl_3$ NCs. Above this s-type band, we find three unoccupied bands with $3d_{xy}$, $3d_{yz}$, and $3d_{xz}$ character. However, on-site transitions between these and the VB-top states are suppressed because of the opposite spins. In contrast, r-$CsMnCl_3$ is a direct band gap material, and its CB edge states are mainly contributed by d-orbitals. Specifically, these unoccupied orbitals and the VB-top 3d orbitals are centered at the nearest-neighboring Mn^{2+} cations and have the same spin. This would establish a charge-transfer electronic-transition channel that involves two nearest-neighboring Mn^{2+} ions. It is similar to the case of emissive $CsMnBr_3$ (which has a similar crystal structure as r-$CsMnCl_3$), whose band edges are primarily composed of Mn d orbitals.[37] The d−d electronic excitations in the AFM r-$CsMnCl_3$ between the band edges are spin-allowed (as both are spin-

https://doi.org/10.1021/acsanm.2c04342
ACS Appl. Nano Mater. 2023, 6, 953−965

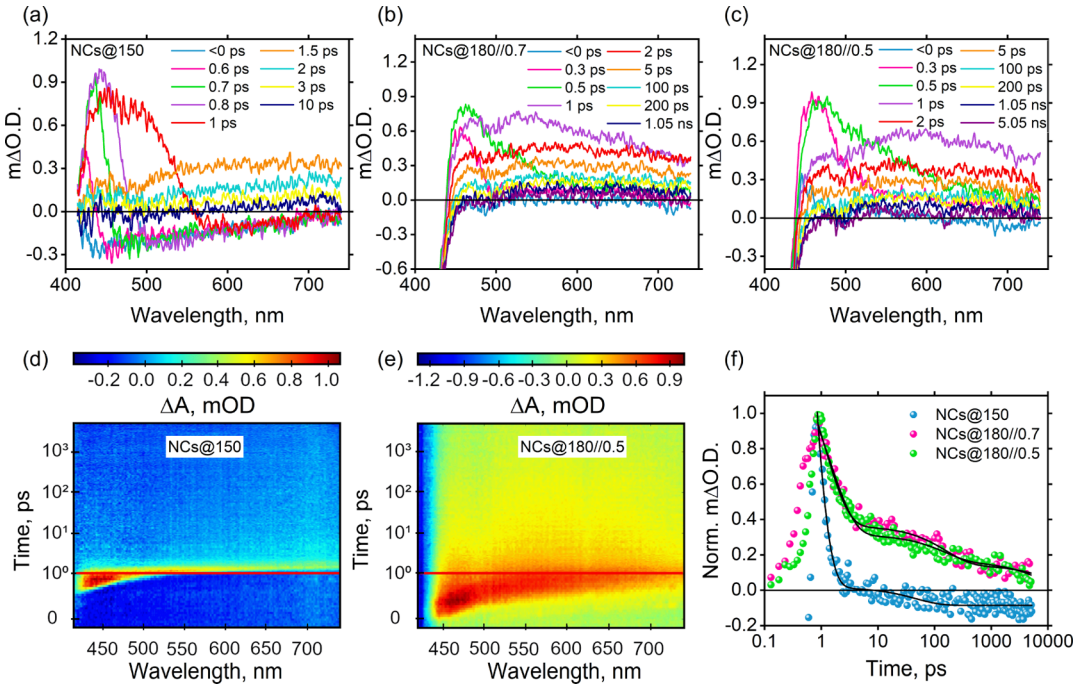

Figure 6. Ultrafast TA spectra of $CsMnCl_3$ (a) 150@NCs, (b) 180@NCs//0.7, and (c) 180@NCs//0.5 excited at 300 nm with an excitation power of 80 μW. TA mapping images of $CsMnCl_3$ (d) 150@NCs and (e) 180@NCs//0.5. (f) TA decays of $CsMnCl_3$ NCs monitored at 445 nm for 150@NCs and 550 nm for 180@NCs//0.7 and 180@NCs//0.5. Solid lines present the fitting results with a triexponential function: $\Delta O.D. = A_1\exp\left(-\frac{t}{\tau_1}\right) + A_2\exp\left(-\frac{t}{\tau_2}\right) + A_3\exp\left(-\frac{t}{\tau_3}\right)$ for 180@NCs//0.7 and 180@NCs//0.5 and with a bi-exponential function: $\Delta O.D. = A_1\exp\left(-\frac{t}{\tau_1}\right) + A_2\exp\left(-\frac{t}{\tau_2}\right)$ for 150@NCs, respectively, ΔO.D. is the change of optical density.

up orbitals), and the local symmetry breaking partially relaxes the Laporte forbidden nature of the transitions.

Electronic transitions between VB and CB edge states of c-$CsMnCl_3$ are prohibited by orbital symmetry and spin. Spin does not prohibit the VB maximum to CB minimum transition in r-$CsMnCl_3$. However, the DFT-HSE band gap of r-$CsMnCl_3$ is larger than the experimentally observed emission energy and the experimentally measured onset of absorption. We speculate that the involvement of defects, exciton self-trapping, or an as of now unresolved mechanism is responsible for the experimentally observed redshift in the emission spectrum. We can, however, provide further insight into the characteristics of the emissive feature by investigating the PLE spectrum of the NCs monitored at the emission maximum of 670 nm. It features six peaks at 335, 355, 370, 420, 450, and 530 nm, in addition to the 280 nm band gap feature (Figure 4a). Transitions corresponding to these six peaks might be of d orbital nature.[6,38] We assigned these peaks with the help of the crystal field theory and Tanabe-Sugano (T-S) diagram.[38] The Racah's Parameter (B) (which measures the Mn−Cl bond strength) and the crystal field splitting energy (Δ) (which quantifies the strength of the crystal field and hence the degree of splitting of the d-energy levels) were determined from the lowest d−d transitions at 450 and 530 nm and were found to be 770 cm^{-1} (0.095 eV) and 8601 cm^{-1} (1.06 eV), respectively. These values are in the range typically found for the electronic transitions in octahedrally coordinated manganese compounds.[6,38] The assignment of all peaks of the PLE spectrum is depicted in Figure 4a and summarized in Table S5. The calculated values of the B and Δ parameters are given in Table S5. Also, the PL spectra collected at different excitation wavelengths exhibit the same shape and the peak wavelength, which suggests that the emission occurs from the relaxation of the same excited state regardless of the excitation energy (Figure S5a). Further electronic-structure theory calculations, which are beyond the scope of this work, can utilize our PLE analysis to identify the source of the red emission.

The emission maximum and the fwhm values of the r-$CsMnCl_3$ NCs are identical (see Table S4) regardless of the injection temperature (180 or 200 °C) or the Mn/Cs ratio. This indicates that the changes in the average size (10.8−15.5 nm) of the emissive NCs have no effect on the position and shape of the emission. The optimized Mn/Cs molar ratio of 0.5 (180@NCs//0.5) leads to the highest PLQY of 40%, while the PLQY of 180@NCs//0.7 is around 12%, and an excess amount of injected Cs-oleate results in a lower PLQY of 24% (180@NCs//0.35). We observe that 180@NCs//0.5 exhibits the longest Mn−Mn distance of 3.52 Å, larger than 3.13 and 3.17 Å for 180@NCs//0.7 and 180@NCs//0.35 samples, respectively, precisely following their PLQY trend. The PLQY dependency on the separation between metal polyhedra was also observed in other low-dimensional Pb-free perovskites.[39] Additionally, the influence of surface traps on the PLQY of the NCs cannot be ignored. Hao et al. showed that the passivation of surface traps by chloride ions is necessary to improve the PLQY of the $CsMnCl_3$ NCs.[8] Subsequently, the radiative recombination is improved as observed from the TRPL decay of the NCs. Furthermore, the PLQY of the r-$CsMnCl_3$ NCs is dependent on the excitation wavelength (Figure 4c). The wavelength dependence of PLQY follows the d−d peak intensity variation in the PLE spectrum (Figure 4a), that is, the excitation wavelength corresponding to the most intense d−d peak (420 nm) leads to the highest PLQY. The relative PLE intensity of the d−d peaks typically indicates the relative

https://doi.org/10.1021/acsanm.2c04342
ACS Appl. Nano Mater. 2023, 6, 953−965

strength of the corresponding transitions, in turn, suggesting that the PLQY is maximum through the excitation of most prominent d−d transition of the system, similar to the case of other manganese halides.[40]

The TRPL decay profile of r-$CsMnCl_3$ NCs was fitted with a biexponential function as shown in Figure 4d. The average PL lifetime of the NCs is around 240 μs, which is in the same order of magnitude as the bulk $CsMnCl_3$[27] and the NCs reported earlier.[8,11] Interestingly, Bakr and co-workers demonstrated picosecond PL lifetime for the $CsMnBr_3$ NCs in contrast to microsecond lifetime observed for the same NCs in another report.[6,7] The variation in the PL lifetime can be correlated with the variation in the Mn−Mn distance—the shorter the distance, the faster the PL decay.[6,27] The Mn−Mn distance of our r-$CsMnCl_3$ NCs varies between 3.12 and 3.52 Å, and the corresponding PL lifetime is a few hundred microseconds. By contrast, organic−inorganic manganese halides with a similar Mn−Mn distance of 3.38 Å exhibited a PL lifetime of only a few nanoseconds.[41] Owing to high electron-phonon coupling in low-dimensional metal halides,[42] we anticipate that an intermediate electronic excited state, such as a self-trapped exciton (STE) state, causes the extension of the excited-state decay time in the case of r-$CsMnCl_3$ NCs.[7]

STE Formation in r-$CsMnCl_3$ NCs. To verify the formation of STE in the excited state of r-$CsMnCl_3$ NCs, ultrafast TA measurements were conducted on as-synthesized $CsMnCl_3$ NC dispersions. Figure 6a−c shows the TA spectra of c-$CsMnCl_3$ NCs (150@NCs) and r-$CsMnCl_3$ NCs (180@NCs//0.7 and 180@NCs//0.5) excited at 300 nm. A broad positive photoinduced absorption (PIA) band with a long tail toward 750 nm is detected for both 180@NCs//0.7 and 180@NCs//0.5 compared to the narrow PIA band with a short tail up to about 560 nm detected for 150@NCs (Figure S6). We assign this broad PIA band to the STE state, as observed for other Pb-free halide perovskite NCs involving STEs.[43,44] The evolution of the signal in the 2D TA mapping image (Figure 6e) of 180@NCs//0.5 shows a clear redshift, particularly after 1.5 ps, unlike the 150@NCs case. The comparison between the cubic and rhombohedral cases (Figure 6d) further clarifies an STE effect in the r-$CsMnCl_3$ NCs. Figure 6f compares the TA decays monitored at 445 nm for 150@NCs and 550 nm for 180@NCs//0.7 and 180@NCs//0.5, which were fitted well with biexponential and triexponential functions, respectively (see Table 1). We assign the two fast components (τ_1 < 2 ps and τ_2 < 200 ps) to the carrier-trapping process and energy-transfer process, respectively, and the slow component (τ_3 > 8 ns) to the STE-related radiative recombination.[45] On the other hand, the TA decay of c-$CsMnCl_3$ NCs (150@NCs) shows a negligible slow component instead, presenting a negative signal. The r-$CsMnCl_3$ NCs (180@NCs//0.7 and 180@NCs//0.5) show a similar long decay lifetime (>8 ns) corresponding to the STE state. Therefore, the structural transition from the cubic phase to the rhombohedral phase induced by the increase of the injection temperature indeed triggers the facile distortion of $MnCl_6$ octahedra in the excited state, which results in the observed STE effect. This is consistent with the ultrafast exciton self-trapping observed in low-dimensional metal halides (1D r-$CsMnCl_3$ NCs in this case) as the potential barrier that exists for the distortion of metal halide polyhedra is much lower than for 3D metal halides (c-$CsMnCl_3$ NCs in this case).[42] We thus speculate that the STE states for r-$CsMnCl_3$ form in the excited state, eventually enhancing the observed red emission, similar to Mn-doped Pb-free double-perovskite NCs.[46] It should be noted here that STE generation does not take place when excited with 370 or 420 nm, that is, below the band gap of the NCs (see Figure S6). It is consistent with the fact that excitation energy a little higher than the band gap is necessary to pump the electrons into the free-carrier or free-exciton state to cause the carrier self-trapping.

Table 1. Summary of Fitting Results of TA Decay Curves of $CsMnCl_3$ NCs

sample	A_1 (%)	τ_1 (ps)	A_2 (%)	τ_2 (ps)	A_3 (%)	τ_3 (ps)
150@NCs	95.8	0.4	4.2	47.1		
180@NCs//0.7	70.9	1.5	10.6	152.7	18.5	8026.8
180@NCs//0.5	71.8	1.1	11.2	161.7	17.0	8525.1

To estimate the exciton binding energy of r-$CsMnCl_3$ NCs, we performed a LTPL characterization on the strongly emitting sample (180@NCs//0.5). PL maximum of the sample gradually red-shifted from 655 nm at room temperature to ∼680 nm at nearly 110 K (Figure 7a). The blue-shifted emission at high temperatures can be ascribed to the lattice expansion. This trend is similar to that of LHP NCs and bulk $CsMnCl_3$ thin films but opposite to that of conventional semiconductors.[27,47] However, the PL maximum of the sample undergoes a small blueshift to 673 nm when cooled below 100 K. Such spinodal nature of the PL peak position with decreasing temperature has been ascribed to Mn−Mn magnetic coupling.[11] As expected, the PL intensity increases as the temperature decreases up to 100 K owing to the emission thermal quenching effect (Figure 7b,c).[48] Below 100 K, the intensity drops slightly.

The temperature-dependent PL quenching of the r-$CsMnCl_3$ NCs (100−300 K) can be expressed via the following equation

$$I(T) = \frac{I_0}{1 + A\, e^{-E_b/k_B T}}$$

where $I(T)$ and I_0 are the PL intensities at temperatures T and 0 K, respectively, E_b is the exciton binding energy, and k_B is the Boltzmann constant. By fitting the PL quenching data using the above equation, an exciton binding energy (E_b) value of 100 ± 18 meV is extracted (Figure 7b), which closely matches the earlier reported value (81.36 meV).[8] The binding energy of 100 meV is higher than that of 3D LHPs and comparable to those of all-inorganic 1D lead-free halide perovskites or quasi-2D organic−inorganic hybrid perovskites.[49−51] A high E_b value indicates strong confinement of the excitons in the r-$CsMnCl_3$ NCs, which might explain its high PLQY. The fwhm of the emission decreases from 69 to 52 meV when the sample cools down from 293 to 50 K (Figure S7), consistent with the earlier studies on the NCs.[8,11] The gradual drop in the fwhm of the NCs with decreasing temperature suggests reduced exciton phonon coupling strength (lattice vibrations), which contributes to the increased integrated PL intensity (Figure 7c).[8,11]

Structural and Emission Stabilities of $CsMnCl_3$ NCs. We assessed the structural stability of the $CsMnCl_3$ NCs in a film form and their PL stability in hexane dispersions. The XRD patterns of c- and r-$CsMnCl_3$ NCs films stored and measured in the ambient conditions (in darkness, RH ∼ 40%, T = 25 °C) were collected as a function of time (Figure 8a). The r-$CsMnCl_3$ NCs display the same XRD pattern before and after 3 months, suggesting the long-term structural stability in

https://doi.org/10.1021/acsanm.2c04342
ACS Appl. Nano Mater. 2023, 6, 953−965

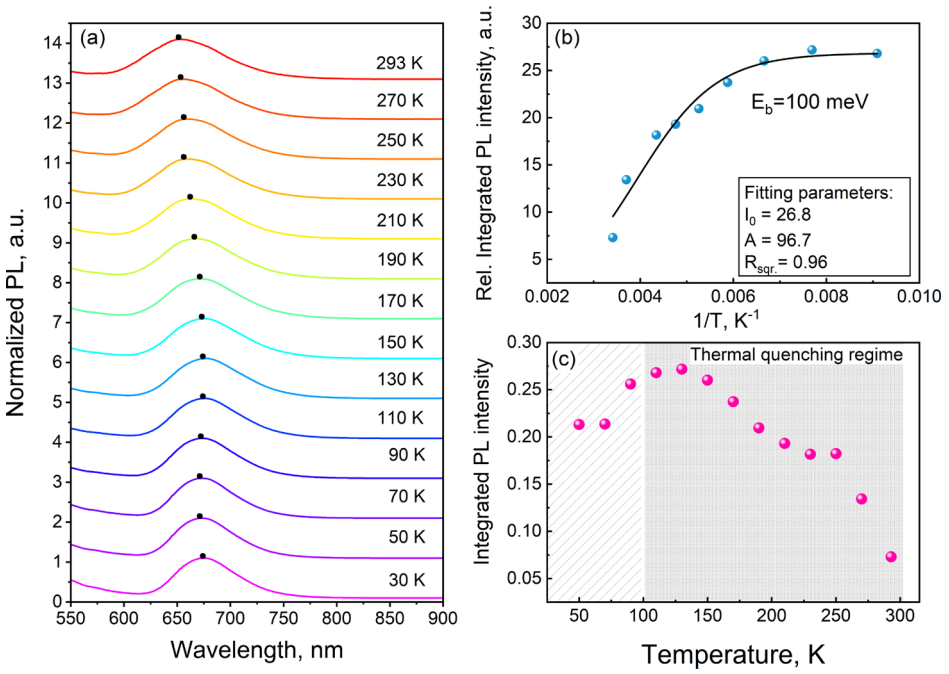

Figure 7. (a) Normalized LTPL spectra of r-$CsMnCl_3$ NCs excited at 380 nm. The sample was initially cooled down up to 30 K, followed by a gradual increase of the temperature toward room temperature with 20 K ramp. The PL maxima are marked with black dots to guide the eye. (b,c) Variation of the integrated PL intensity of r-$CsMnCl_3$ NCs as a function of temperature and determination of the exciton binding energy.

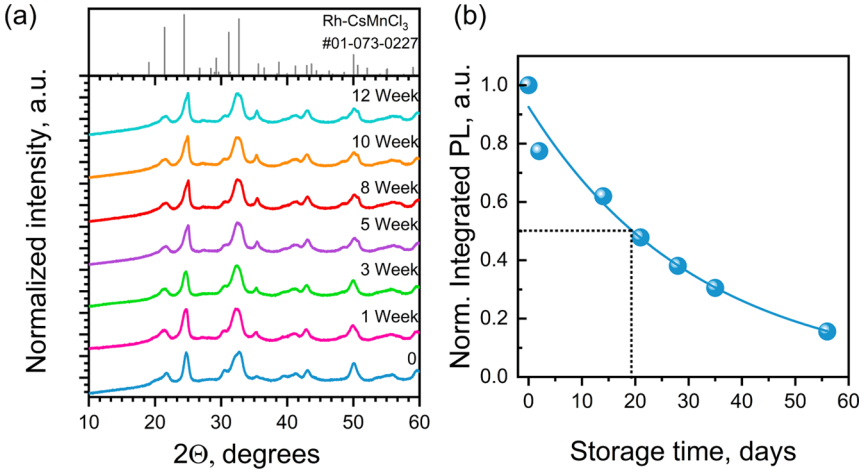

Figure 8. (a) Storage time-dependent XRD patterns of r-$CsMnCl_3$ NCs. (b) Relative integrated PL intensity of the NCs (solid line is to guide the eye, and dashed lines represent drop till 50% from the initial value).

ambient conditions of the r-$CsMnCl_3$ NCs without additional treatments or encapsulation, unlike the red-emissive $CsPbI_3$ NCs.[3,52,53] On the other hand, nonemissive c-$CsMnCl_3$ NCs (150@NCs) do not retain their original XRD pattern already after 9 weeks of storage in air (Figure S8). The Rietveld refinement performed on the aged 150@NCs pattern shows that most of c-$CsMnCl_3$ decomposes into CsCl (Figure S8). Hence, the rhombohedral structure of $CsMnCl_3$ NCs is energetically more favorable than their cubic structure, as supported by our DFT calculations as well as previous studies.[24] Notably, the r-$CsMnCl_3$ NCs retain >70% of their original PLQY after a week in the air (Figure 8b), demonstrating improved luminescence stability compared to the reported $CsMnCl_3$ and Zn-doped $CsMnCl_3$ NCs (which preserved only 10.1 and 51.7% of their initial PLQY, respectively).[8] However, the PL efficiency of the r-$CsMnCl_3$ NCs gradually decreases and reaches 50 and 5% of its initial value in the air after 20 and 55 days, respectively. The TEM images of the aged sample show a partial agglomeration of the NCs (Figure S9). This introduces new surface and structural defects that can act as additional recombination channels and possibly cause or contribute to the luminescence quenching. This may be attributed to the striping of the protective ligand shells from the NC surface.[54] Consequently, ligand engineering may tackle this issue and prolong the PL stability of the NCs through improved surface passivation. A dedicated follow-up study could focus on this direction.

$CsMnCl_3$ NCs for LSC Applications: A Proof-of-Concept Demonstration. Recent advances in the building-integrated photovoltaics demonstrated a new possible way of sunlight harvesting, namely LSCs. The main idea of this concept is to encapsulate the luminescent material in a

https://doi.org/10.1021/acsanm.2c04342
ACS Appl. Nano Mater. 2023, 6, 953−965

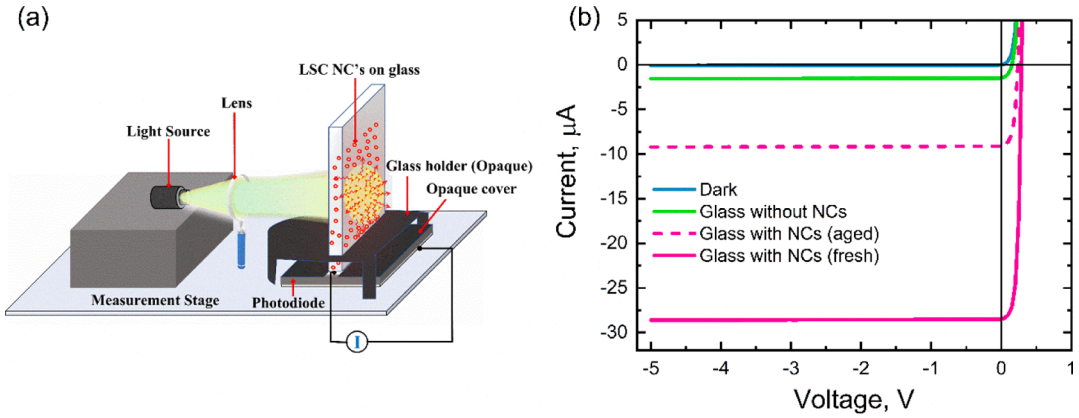

Figure 9. (a) Schematic illustration of the experimental setup. The proof-of-concept device consists of a silicon photodiode that is placed directly under the edge of a miniature glass window with embedded NCs. (b) *I*−*V* characteristics of the Si photodiode with different glass configurations including an aged (11 weeks) NC film. Dark current is a few nA.

polymer composite or glass and embed it in the window. The deployed LSC will absorb part of the sun light arriving at the window and then re-emit it at a longer wavelength. Higher than air refractive index glass will act as a waveguide and direct most of the emitted light to the edges, where the light is converted into electricity via solar cells. The high PLQY of the LHP NCs is appealing for this application. However, apart from the lead toxicity and poor stability in ambient conditions, LHP NCs typically exhibit small Stokes shifts leading to reabsorption effects, which are detrimental for LSCs and limit their scalability. To our knowledge, only Bi-doped $Cs_2Ag_{0.4}Na_{0.6}InCl_6$ NCs were found to be efficient emitters in LSCs due to their PLQY of 38%, broad emission, and low reabsorption.[55]

The above-discussed properties of $CsMnCl_3$ NCs, namely, the Stokes-shifted luminescence in the visible region with a 40% QY and fairly good stability in the air, suggest that they could have potential as active material in LSC devices. To explore this, a dedicated experimental setup presented in Figure 9a was constructed. The details of the setup are described in the Experimental section. Figure 9b shows the measured *I*−*V* characteristics of the photodiode (i) in the dark (blue curve), (ii) under illumination with a standard glass (green curve), and (iii) under illumination with an NC-coated glass (red curve). In the dark, the photodiode exhibits rectifying characteristics with a very low current of a few nA. The benefit from the PL of the NC film is evident as the photocurrent for an NC thin film-coated glass is an order of magnitude higher than for a glass without NCs (and approximately 4 orders of magnitude higher than the dark current). This result demonstrates the potential of the $CsMnCl_3$ NCs to produce electricity when coupled in an actual LSC device.

Additionally, we examined how the aging of the $CsMnCl_3$ NC film affects the photocurrent by measuring the same film after 11 weeks of aging in air (Figure 9b). Evidently, due to the degradation of the PL properties of the NCs (Figure 8b), the measured photocurrent is nearly 3 times lower than the initial value (but still higher than the reference). This experiment provides additional confirmation that the observed photocurrent is caused by the luminescence of the NCs instead of mere light scattering by the film components that in turn should not be affected by the stability of the NCs. It should be noted that the NC films were completely unencapsulated here; therefore, LSCs evidentially demonstrate a drop in the performance. However, even in these conditions, the photocurrent was still generated, which allows us to speculate that considerably longer stability is expected for the NCs integrated into a protective matrix. Therefore, we believe that $CsMnCl_3$ NCs is a promising candidate for LSC applications among other lead-free NCs.[55]

CONCLUSIONS

In summary, we have successfully synthesized 3D and 1D $CsMnCl_3$ NCs, namely, cubic and rhombohedral phases, by tuning the temperature of a hot injection colloidal synthesis. The DFT-calculated electronic band structures of c-$CsMnCl_3$ and r-$CsMnCl_3$ NCs demonstrate that they have indirect and direct band gaps, respectively. This may explain their distinct PL properties; c-$CsMnCl_3$ NCs are nonemissive, while r-$CsMnCl_3$ NCs that possess allowed electronic transitions between the VB and CB edge states display bright red luminescence centered at 670 nm. Furthermore, the luminescence stability of the NCs in the air is improved compared to earlier reports. However, much higher stability is essential to realize optoelectronic devices, like the proof-of-concept example of LSCs. We suggest that ligand engineering, with capping ligands that reduce the surface defects while strongly binding to the NC surface, could be a promising future approach to simultaneously improve the PLQY and luminescence stability.

ASSOCIATED CONTENT

Supporting Information

The Supporting Information is available free of charge at https://pubs.acs.org/doi/10.1021/acsanm.2c04342.

Photographs of the NCs; TEM images and size distribution of the NCs; Rietveld refinement parameters of $CsMnCl_3$ NCs; Tauc plots; injection temperature-dependent absorption and PL spectra and TRPL decay curves; excitation wavelength-dependent PL spectra; excitation wavelength-dependent TA spectra and decay curves; temperature-dependent fwhm variation; and stability studies of $CsMnCl_3$ NCs (PDF)

https://doi.org/10.1021/acsanm.2c04342
ACS Appl. Nano Mater. 2023, 6, 953−965

AUTHOR INFORMATION

Corresponding Authors

G. Krishnamurthy Grandhi − *Hybrid Solar Cells, Faculty of Engineering and Natural Sciences, Tampere University, FI-33014 Tampere, Finland*; Email: murthy.grandhi@tuni.fi

Paola Vivo − *Hybrid Solar Cells, Faculty of Engineering and Natural Sciences, Tampere University, FI-33014 Tampere, Finland*; orcid.org/0000-0003-2872-6922; Email: paola.vivo@tuni.fi

Authors

Anastasia Matuhina − *Hybrid Solar Cells, Faculty of Engineering and Natural Sciences, Tampere University, FI-33014 Tampere, Finland*

Fang Pan − *Electronic Materials Research Laboratory, Key Laboratory of the Ministry of Education and International Center for Dielectric Research, School of Electronic Science and Engineering & International Joint Laboratory for Micro/Nano Manufacturing and Measurement Technology, Xi'an Jiaotong University, 710049 Xi'an, China*

Maning Liu − *Hybrid Solar Cells, Faculty of Engineering and Natural Sciences, Tampere University, FI-33014 Tampere, Finland*; orcid.org/0000-0001-9875-0966

Harri Ali-Löytty − *Surface Science Group, Photonics Laboratory, Tampere University, FI-33014 Tampere, Finland*; orcid.org/0000-0001-8746-7268

Hussein M. Ayedh − *Department of Electronics and Nanoengineering, Aalto University, FI-02150 Espoo, Finland*

Antti Tukiainen − *Faculty of Engineering and Natural Sciences, Tampere University, FI-33014 Tampere, Finland*

Jan-Henrik Smått − *Laboratory of Molecular Science and Engineering, Åbo Akademi University, FI-20500 Turku, Finland*

Ville Vähänissi − *Department of Electronics and Nanoengineering, Aalto University, FI-02150 Espoo, Finland*; orcid.org/0000-0002-2681-5609

Hele Savin − *Department of Electronics and Nanoengineering, Aalto University, FI-02150 Espoo, Finland*; orcid.org/0000-0003-3946-7727

Jingrui Li − *Electronic Materials Research Laboratory, Key Laboratory of the Ministry of Education and International Center for Dielectric Research, School of Electronic Science and Engineering & International Joint Laboratory for Micro/Nano Manufacturing and Measurement Technology, Xi'an Jiaotong University, 710049 Xi'an, China*

Patrick Rinke − *Department of Applied Physics, Aalto University, FI-00076 Aalto, Finland*; orcid.org/0000-0003-1898-723X

Complete contact information is available at: https://pubs.acs.org/10.1021/acsanm.2c04342

Author Contributions

The manuscript was written through contributions of all authors. All authors have given approval to the final version of the manuscript.

Notes

The authors declare no competing financial interest.

ACKNOWLEDGMENTS

Dr. Mari Honkanen and Tampere Microscopy Center are gratefully acknowledged for the TEM images. This work is part of the Academy of Finland Flagship Programme, Photonics Research and Innovation (PREIN), decision No 320165. P.V. acknowledges the support of Jane & Aatos Erkko foundation (project "SOL-TECH"). M.L. thanks the Finnish Cultural Foundation (00210670) for funding. H.M.A. and V.V. acknowledge the financial support of the Academy of Finland (#331313). H.M.A., V.V., and H.S. acknowledge the provision of facilities and technical support by Micronova Nanofabrication Centre and Nanomicroscopy Centre in Espoo, Finland within the OtaNano research infrastructure at Aalto University. The assistance provided by Dr. Diao Li regarding the optical components and their setup for the proof-of-concept photodiode $I-V$ measurements is highly appreciated.

REFERENCES

(1) Protesescu, L.; Yakunin, S.; Bodnarchuk, M. I.; Krieg, F.; Caputo, R.; Hendon, C. H.; Yang, R. X.; Walsh, A.; Kovalenko, M. V. Nanocrystals of Cesium Lead Halide Perovskites ($CsPbX_3$, X = Cl, Br, and I): Novel Optoelectronic Materials Showing Bright Emission with Wide Color Gamut. *Nano Lett.* **2015**, *15*, 3692−3696.

(2) Dutta, A.; Behera, R. K.; Pal, P.; Baitalik, S.; Pradhan, N. Near-unity Photoluminescence Quantum Efficiency for All $CsPbX_3$ (X= Cl, Br, and I) Perovskite Nanocrystals: A Generic Synthesis Approach. *Angew. Chem., Int. Ed.* **2019**, *58*, 5552−5556.

(3) Dutta, A.; Pradhan, N. Phase-Stable Red-Emitting $CsPbI_3$ Nanocrystals: Successes and Challenges. *ACS Energy Lett.* **2019**, *4*, 709−719.

(4) Li, X.; Gao, X.; Zhang, X.; Shen, X.; Lu, M.; Wu, J.; Shi, Z.; Colvin, V. L.; Hu, J.; Bai, X.; Yu, W. W.; Zhang, Y. Lead-Free Halide Perovskites for Light Emission: Recent Advances and Perspectives. *Adv. Sci.* **2021**, *8*, 2003334.

(5) Gao, F.; Zhu, X.; Feng, Q.; Zhong, W.; Liu, W.; Xu, H.; Liu, Y. Deep-Blue Emissive $Cs_3Cu_2I_5$ Perovskites Nanocrystals with 96.6% Quantum Yield via InI_3-Assisted Synthesis for Light-Emitting Device and Fluorescent Ink Applications. *Nano Energy* **2022**, *98*, 107270.

(6) Almutlaq, J.; Mir, W. J.; Gutiérrez-Arzaluz, L.; Yin, J.; Vasylevskyi, S.; Maity, P.; Liu, J.; Naphade, R.; Mohammed, O. F.; Bakr, O. M. $CsMnBr_3$: Lead-Free Nanocrystals with High Photoluminescence Quantum Yield and Picosecond Radiative Lifetime. *ACS Mater. Lett.* **2021**, *3*, 290−297.

(7) Kong, Q.; Yang, B.; Chen, J.; Zhang, R.; Liu, S.; Zheng, D.; Zhang, H.; Liu, Q.; Wang, Y.; Han, K. Phase Engineering of Cesium Manganese Bromides Nanocrystals with Color-Tunable Emission. *Angew. Chem., Int. Ed.* **2021**, *133*, 19805−19811.

(8) Hao, X.; Liu, H.; Ding, W.; Zhang, F.; Li, X.; Wang, S. Zn^{2+}-Doped Lead-Free $CsMnCl_3$ Nanocrystals Enable Efficient Red Emission with a High Photoluminescence Quantum Yield. *J. Phys. Chem. Lett.* **2022**, *13*, 4688−4694.

(9) Gao, D.; Qiao, B.; Xu, Z.; Song, D.; Song, P.; Liang, Z.; Shen, Z.; Cao, J.; Zhang, J.; Zhao, S. Postsynthetic, Reversible Cation Exchange between Pb^{2+} and Mn^{2+} in Cesium Lead Chloride Perovskite Nanocrystals. *J. Phys. Chem. C* **2017**, *121*, 20387−20395.

(10) Fang, G.; Chen, D.; Zhou, S.; Chen, X.; Lei, L.; Zhong, J.; Ji, Z. Reverse Synthesis of $CsPb_xMn_{1-x}(Cl/Br)_3$ Perovskite Quantum Dots from $CsMnCl_3$ Precursors through Cation Exchange. *J. Mater. Chem. C* **2018**, *6*, 5908−5915.

(11) Guan, L. Q.; Shi, S.; Niu, X. W.; Guo, S. C.; Zhao, J.; Ji, T. M.; Dong, H.; Jia, F. Y.; Xiao, J. W.; Sun, L. D.; Yan, C. H. All-Inorganic Manganese-Based $CsMnCl_3$ Nanocrystals for X-Ray Imaging. *Adv. Sci.* **2022**, *9*, No. e2201354.

(12) Chen, J.-K.; Zhao, Q.; Shirahata, N.; Yin, J.; Bakr, O. M.; Mohammed, O. F.; Sun, H.-T. Shining Light on the Structure of Lead Halide Perovskite Nanocrystals. *ACS Mater. Lett.* **2021**, *3*, 845−861.

(13) Xiao, G.; Cao, Y.; Qi, G.; Wang, L.; Liu, C.; Ma, Z.; Yang, X.; Sui, Y.; Zheng, W.; Zou, B. Pressure Effects on Structure and Optical Properties in Cesium Lead Bromide Perovskite Nanocrystals. *J. Am. Chem. Soc.* **2017**, *139*, 10087−10094.

(14) Luo, J.; Wang, X.; Li, S.; Liu, J.; Guo, Y.; Niu, G.; Yao, L.; Fu, Y.; Gao, L.; Dong, Q.; Zhao, C.; Leng, M.; Ma, F.; Liang, W.; Wang,

L.; Jin, S.; Han, J.; Zhang, L.; Etheridge, J.; Wang, J.; Yan, Y.; Sargent, E. H.; Tang, J. Efficient and Stable Emission of Warm-White Light from Lead-Free Halide Double Perovskites. *Nature* **2018**, *563*, 541−545.
(15) Ahmed, G. H.; Liu, Y.; Bravić, I.; Ng, X.; Heckelmann, I.; Narayanan, P.; Fernández, M. S.; Monserrat, B.; Congreve, D. N.; Feldmann, S. Luminescence Enhancement Due to Symmetry Breaking in Doped Halide Perovskite Nanocrystals. *J. Am. Chem. Soc.* **2022**, *144*, 15862−15870.
(16) Schmitt, T.; Bourelle, S.; Tye, N.; Soavi, G.; Bond, A. D.; Feldmann, S.; Traore, B.; Katan, C.; Even, J.; Dutton, S. E.; Deschler, F. Control of Crystal Symmetry Breaking with Halogen-Substituted Benzylammonium in Layered Hybrid Metal-Halide Perovskites. *J. Am. Chem. Soc.* **2020**, *142*, 5060−5067.
(17) Fu, R.; Chen, Y.; Yong, X.; Ma, Z.; Wang, L.; Lv, P.; Lu, S.; Xiao, G.; Zou, B. Pressure-Induced Structural Transition and Band Gap Evolution of Double Perovskite $Cs_2AgBiBr_6$ Nanocrystals. *Nanoscale* **2019**, *11*, 17004−17009.
(18) Leng, J.; Wang, T.; Tan, Z.-K.; Lee, Y.-J.; Chang, C.-C.; Tamada, K. Tuning the Emission Wavelength of Lead Halide Perovskite NCs via Size and Shape Control. *ACS Omega* **2022**, *7*, 565−577.
(19) Dutta, A.; Behera, R. K.; Dutta, S. K.; Das Adhikari, S.; Pradhan, N. Annealing $CsPbX_3$ (X = Cl and Br) Perovskite Nanocrystals at High Reaction Temperatures: Phase Change and Its Prevention. *J. Phys. Chem. Lett.* **2018**, *9*, 6599−6604.
(20) Dutta, A.; Dutta, S. K.; Das Adhikari, S.; Pradhan, N. Phase-Stable $CsPbI_3$ Nanocrystals: The Reaction Temperature Matters. *Angew. Chem., Int. Ed.* **2018**, *57*, 9083−9087.
(21) Matuhina, A.; Grandhi, G. K.; Liu, M.; Smått, J. H.; Viswanath, N. S. M.; Ali-Löytty, H.; Lahtonen, K.; Vivo, P. Octahedral Distortion Driven by $CsPbI_3$ nanocrystal Reaction Temperature-the Effects on Phase Stability and Beyond. *Nanoscale* **2021**, *13*, 14186−14196.
(22) Protesescu, L.; Yakunin, S.; Kumar, S.; Bär, J.; Bertolotti, F.; Masciocchi, N.; Guagliardi, A.; Grotevent, M.; Shorubalko, I.; Bodnarchuk, M. I.; Shih, C.-J.; Kovalenko, M. V. Dismantling the "Red Wall" of Colloidal Perovskites: Highly Luminescent Formamidinium and Formamidinium−Cesium Lead Iodide Nanocrystals. *ACS Nano* **2017**, *11*, 3119−3134.
(23) Momma, K.; Izumi, F. VESTA 3 for Three-Dimensional Visualization of Crystal, Volumetric and Morphology Data. *J. Appl. Crystallogr.* **2011**, *44*, 1272−1276.
(24) Longo, J. M.; Kafalas, J. A. Effect of Pressure on the Crystal Structure of $CsMnCl_3$ and $RbMnCl_3$. *J. Solid State Chem.* **1971**, *3*, 429−433.
(25) Toso, S.; Akkerman, Q. A.; Martín-García, B.; Prato, M.; Zito, J.; Infante, I.; Dang, Z.; Moliterni, A.; Giannini, C.; Bladt, E.; Lobato, I.; Ramade, J.; Bals, S.; Buha, J.; Spirito, D.; Mugnaioli, E.; Gemmi, M.; Manna, L. Nanocrystals of Lead Chalcohalides: A Series of Kinetically Trapped Metastable Nanostructures. *J. Am. Chem. Soc.* **2020**, *142*, 10198−10211.
(26) Ke, W.; Kanatzidis, M. G. Prospects for Low-Toxicity Lead-Free Perovskite Solar Cells. *Nat. Commun.* **2019**, *10*, 965.
(27) Zhu, X.; Meng, S.; Zhao, Y.; Zhang, S.; Zhang, J.; Yin, C.; Ye, S. Mn^{2+}−Mn^{2+} Magnetic Coupling Effect on Photoluminescence Revealed by Photomagnetism in $CsMnCl_3$. *J. Phys. Chem. Lett.* **2020**, *11*, 9587−9595.
(28) Imran, M.; Caligiuri, V.; Wang, M.; Goldoni, L.; Prato, M.; Krahne, R.; De Trizio, L. D.; Manna, L. Benzoyl Halides as Alternative Precursors for the Colloidal Synthesis of Lead-Based Halide Perovskite Nanocrystals. *J. Am. Chem. Soc.* **2018**, *140*, 2656−2664.
(29) Shamsi, J.; Urban, A. S.; Imran, M.; De Trizio, L. D.; Manna, L. Metal Halide Perovskite Nanocrystals: Synthesis, Post-Synthesis Modifications, and Their Optical Properties. *Chem. Rev.* **2019**, *119*, 3296−3348.
(30) Lassoued, M. S.; Bi, L.-Y.; Wu, Z.; Zhou, G.; Zheng, Y.-Z. Piperidine-Induced Switching of the Direct Band Gaps of Ag (I)/Bi (III) Bimetallic Iodide Double Perovskites. *J. Mater. Chem. C* **2020**, *8*, 5349−5354.
(31) McKechnie, S.; Frost, J. M.; Pashov, D.; Azarhoosh, P.; Walsh, A.; van Schilfgaarde, M. Dynamic Symmetry Breaking and Spin Splitting in Metal Halide Perovskites. *Phys. Rev. B* **2018**, *98*, 85108.
(32) Heyd, J.; Scuseria, G. E.; Ernzerhof, M. Hybrid Functionals Based on a Screened Coulomb Potential. *J. Chem. Phys.* **2003**, *118*, 8207−8215.
(33) Blum, V.; Gehrke, R.; Hanke, F.; Havu, P.; Havu, V.; Ren, X.; Reuter, K.; Scheffler, M. Ab Initio Molecular Simulations with Numeric Atom-Centered Orbitals. *Comput. Phys. Commun.* **2009**, *180*, 2175−2196.
(34) Havu, V.; Blum, V.; Havu, P.; Scheffler, M. Efficient integration for all-electron electronic structure calculation using numeric basis functions. *J. Comput. Phys.* **2009**, *228*, 8367−8379.
(35) Ren, X.; Rinke, P.; Blum, V.; Wieferink, J.; Tkatchenko, A.; Sanfilippo, A.; Reuter, K.; Scheffler, M. Resolution-of-Identity Approach to Hartree−Fock, Hybrid Density Functionals, RPA, MP2 and GW with Numeric Atom-Centered Orbital Basis Functions. *New J. Phys.* **2012**, *14*, 53020.
(36) Levchenko, S. V.; Ren, X.; Wieferink, J.; Johanni, R.; Rinke, P.; Blum, V.; Scheffler, M. Hybrid Functionals for Large Periodic Systems in an All-Electron, Numeric Atom-Centered Basis Framework. *Comput. Phys. Commun.* **2015**, *192*, 60−69.
(37) Bahmani Jalali, H.; Pianetti, A.; Zito, J.; Imran, M.; Campolucci, M.; Ivanov, Y. P.; Locardi, F.; Infante, I.; Divitini, G.; Brovelli, S.; Manna, L.; Di Stasio, F. Cesium Manganese Bromide Nanocrystal Sensitizers for Broadband Vis-to-NIR Downshifting. *ACS Energy Lett.* **2022**, *7*, 1850−1858.
(38) Rodríguez-Lazcano, Y.; Nataf, L.; Rodríguez, F. Electronic Structure and Luminescence of $[(CH_3)_4N]_2MnX_4$ (X= Cl, Br) Crystals at High Pressures by Time-Resolved Spectroscopy: Pressure Effects on the Mn-Mn Exchange Coupling. *Phys. Rev. B: Condens. Matter Mater. Phys.* **2009**, *80*, 085115.
(39) Molokeev, M. S.; Su, B.; Aleksandrovsky, A. S.; Golovnev, N. N.; Plyaskin, M. E.; Xia, Z. Machine Learning Analysis and Discovery of Zero-Dimensional ns^2 Metal Halides toward Enhanced Photoluminescence Quantum Yield. *Chem. Mater.* **2022**, *34*, 537−546.
(40) Morad, V.; Cherniukh, I.; Pöttschacher, L.; Shynkarenko, Y.; Yakunin, S.; Kovalenko, M. V. Manganese(II) in Tetrahedral Halide Environment: Factors Governing Bright Green Luminescence. *Chem. Mater.* **2019**, *31*, 10161−10169.
(41) Peng, H.; Zou, B.; Guo, Y.; Xiao, Y.; Zhi, R.; Fan, X.; Zou, M.; Wang, J. Evolution of the Structure and Properties of Mechanochemically Synthesized Pyrrolidine Incorporated Manganese Bromide Powders. *J. Mater. Chem. C* **2020**, *8*, 6488−6495.
(42) Li, M.; Xia, Z. Recent Progress of Zero-Dimensional Luminescent Metal Halides. *Chem. Soc. Rev.* **2021**, *50*, 2626−2662.
(43) Han, P.; Luo, C.; Yang, S.; Yang, Y.; Deng, W.; Han, K. All-Inorganic Lead-Free 0D Perovskites by a Doping Strategy to Achieve a PLQY Boost from <2 % to 90 %. *Angew. Chem.* **2020**, *59*, 12709−12713.
(44) Liu, M.; Matta, S.; Ali-Löytty, H.; Matuhina, A.; Grandhi, G.; Lahtonen, K.; Russo, P. S.; Vivo, P. Moisture-Assisted near-UV Emission Enhancement of Lead-Free $Cs_4CuIn_2Cl_{12}$ Double Perovskite Nanocrystals. *Nano Lett.* **2021**, *22*, 311−318.
(45) Yang, B.; Han, K. Ultrafast Dynamics of Self-Trapped Excitons in Lead-Free Perovskite Nanocrystals. *J. Phys. Chem. Lett.* **2021**, *12*, 8256−8262.
(46) Han, P.; Zhang, X.; Luo, C.; Zhou, W.; Yang, S.; Zhao, J.; Deng, W.; Han, K. Manganese-Doped, Lead-Free Double Perovskite Nanocrystals for Bright Orange-Red Emission. *ACS Cent. Sci.* **2020**, *6*, 566−572.
(47) Lee, S. M.; Moon, C. J.; Lim, H.; Lee, Y.; Choi, M. Y.; Bang, J. Temperature-Dependent Photoluminescence of Cesium Lead Halide Perovskite Quantum Dots: Splitting of the Photoluminescence Peaks of $CsPbBr_3$ and $CsPb(Br/I)_3$ Quantum Dots at Low Temperature. *J. Phys. Chem. C* **2017**, *121*, 26054−26062.

https://doi.org/10.1021/acsanm.2c04342
ACS Appl. Nano Mater. 2023, 6, 953−965

(48) Liu, M.; Grandhi, G. K.; Matta, S.; Mokurala, K.; Litvin, A.; Russo, S.; Vivo, P. Halide Perovskite Nanocrystal Emitters. *Adv. Photonics Res.* **2021**, *2*, 2000118.
(49) Li, X.; Wu, Y.; Zhang, S.; Cai, B.; Gu, Y.; Song, J.; Zeng, H. $CsPbX_3$ Quantum Dots for Lighting and Displays: Room-temperature Synthesis, Photoluminescence Superiorities, Underlying Origins and White Light-emitting Diodes. *Adv. Funct. Mater.* **2016**, *26*, 2435−2445.
(50) Chen, P.; Bai, Y.; Lyu, M.; Yun, J.; Hao, M.; Wang, L. Progress and Perspective in Low-Dimensional Metal Halide Perovskites for Optoelectronic Applications. *Sol. RRL* **2018**, *2*, 1700186.
(51) Yang, J.; Kang, W.; Liu, Z.; Pi, M.; Luo, L.-B.; Li, C.; Lin, H.; Luo, Z.; Du, J.; Zhou, M.; Tang, X. High-Performance Deep Ultraviolet Photodetector Based on a One-Dimensional Lead-Free Halide Perovskite $CsCu_2I_3$ Film with High Stability. *J. Phys. Chem. Lett.* **2020**, *11*, 6880−6886.
(52) Ushakova, E. V.; Matuhina, A. I.; Sokolova, A. V.; Cherevkov, S. A.; Dubavik, A.; Medvedev, O. S.; Litvin, A. P.; Kurdyukov, D. A.; Golubev, V. G.; Baranov, A. V. Enhanced Stability of the Optical Responses from All-Inorganic Perovskite Nanocrystals Embedded in a Synthetic Opal Matrix. *Nanotechnology* **2019**, *30*, 405206.
(53) Huang, Y.; Luan, W.; Liu, M.; Turyanska, L. DDAB-Assisted Synthesis of Iodine-Rich $CsPbI_3$ Perovskite Nanocrystals with Improved Stability in Multiple Environments. *J. Mater. Chem. C* **2020**, *8*, 2381−2387.
(54) Hills-kimball, K.; Yang, H.; Cai, T.; Wang, J.; Chen, O. Recent Advances in Ligand Design and Engineering in Lead Halide Perovskite Nanocrystals. *Adv. Sci.* **2021**, *8*, 2100214.
(55) Zdražil, L.; Kalytchuk, S.; Langer, M.; Ahmad, R.; Pospíšil, J.; Zmeškal, O.; Altomare, M.; Osvet, A.; Zbořil, R.; Schmuki, P.; Brabec, C. J.; Otyepka, M.; Kment, Š. Transparent and Low-Loss Luminescent Solar Concentrators Based on Self-Trapped Exciton Emission in Lead-Free Double Perovskite Nanocrystals. *ACS Appl. Energy Mater.* **2021**, *4*, 6445−6453.

https://doi.org/10.1021/acsanm.2c04342
ACS Appl. Nano Mater. 2023, 6, 953−965